Science Advances

AAAS

advances.sciencemag.org/cgi/content/full/3/3/e1501645/DC1

Supplementary Materials for

Self-powered integrated microfluidic point-of-care low-cost enabling (SIMPLE) chip

Erh-Chia Yeh, Chi-Cheng Fu, Lucy Hu, Rohan Thakur, Jeffrey Feng, Luke P. Lee

Published 22 March 2017, *Sci. Adv.* **3**, e1501645 (2017)
DOI: 10.1126/sciadv.1501645

The PDF file includes:

Other Supplementary Material for this manuscript includes the following:

(available at advances.sciencemag.org/cgi/content/full/3/3/e1501645/DC1)

- movie S1 (.mov format). User protocol.
- movie S2 (.mov format). Cross section.
- movie S3 (.mov format). Digital plasma separation.
- movie S4 (.mov format). Vacuum battery system.

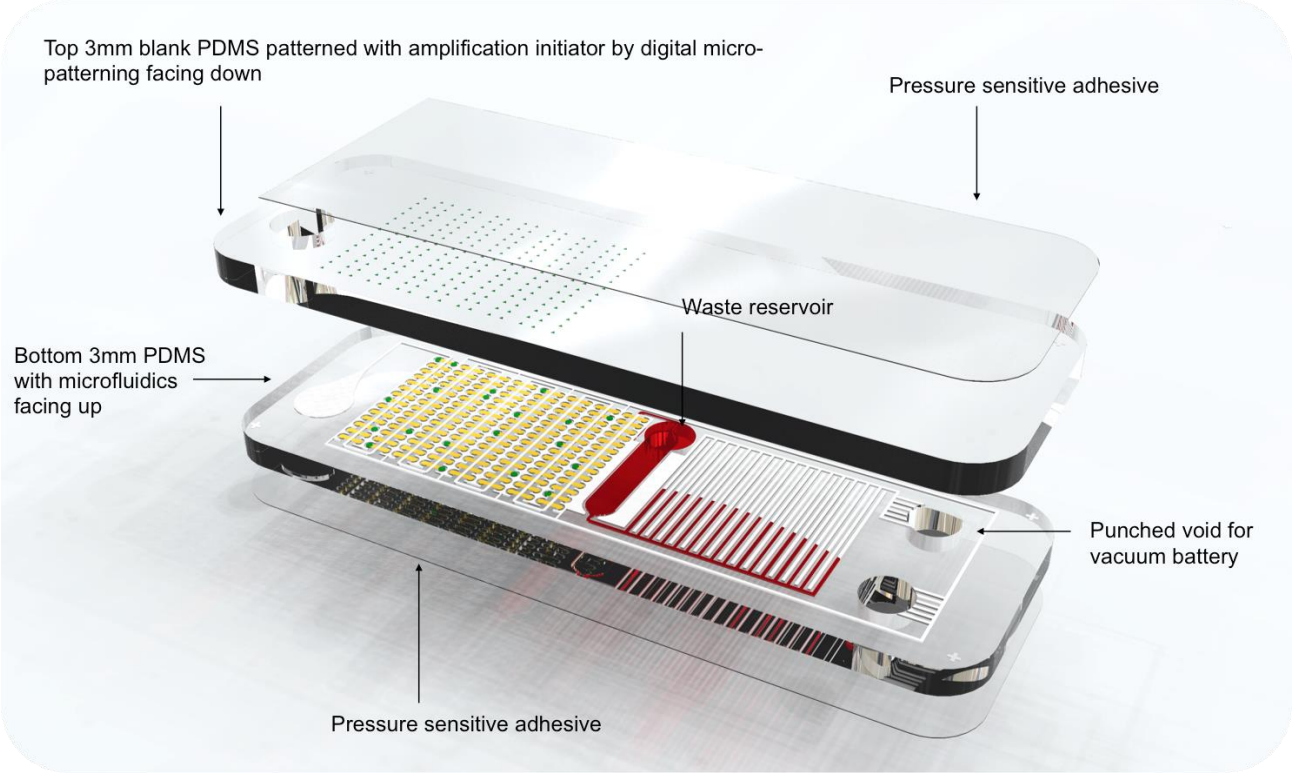

fig. S1. Exploded view of the simple construction. Only two layers of air permeable silicone material (PDMS) are needed. These two layers are bonded together by exposing UV light to the PDMS. The bottom layer consists of the fluidic components; the large waste reservoir and vacuum battery voids were punched with punchers. The top piece is a blank PDMS that has been patterned with amplification initiator (MgOAc) on the bottom-bonding surface. Transparent pressure sensitive adhesive is added on the top and bottom to prevent excess air diffusion from the top and bottom surfaces of PDMS. Microfluidic channels are highlighted with colors to show different functional parts. Red is the blood sample; white are empty channels and vacuum lines. The footprint of this device is 25*75 mm, which is the same as a standard microscope slide.

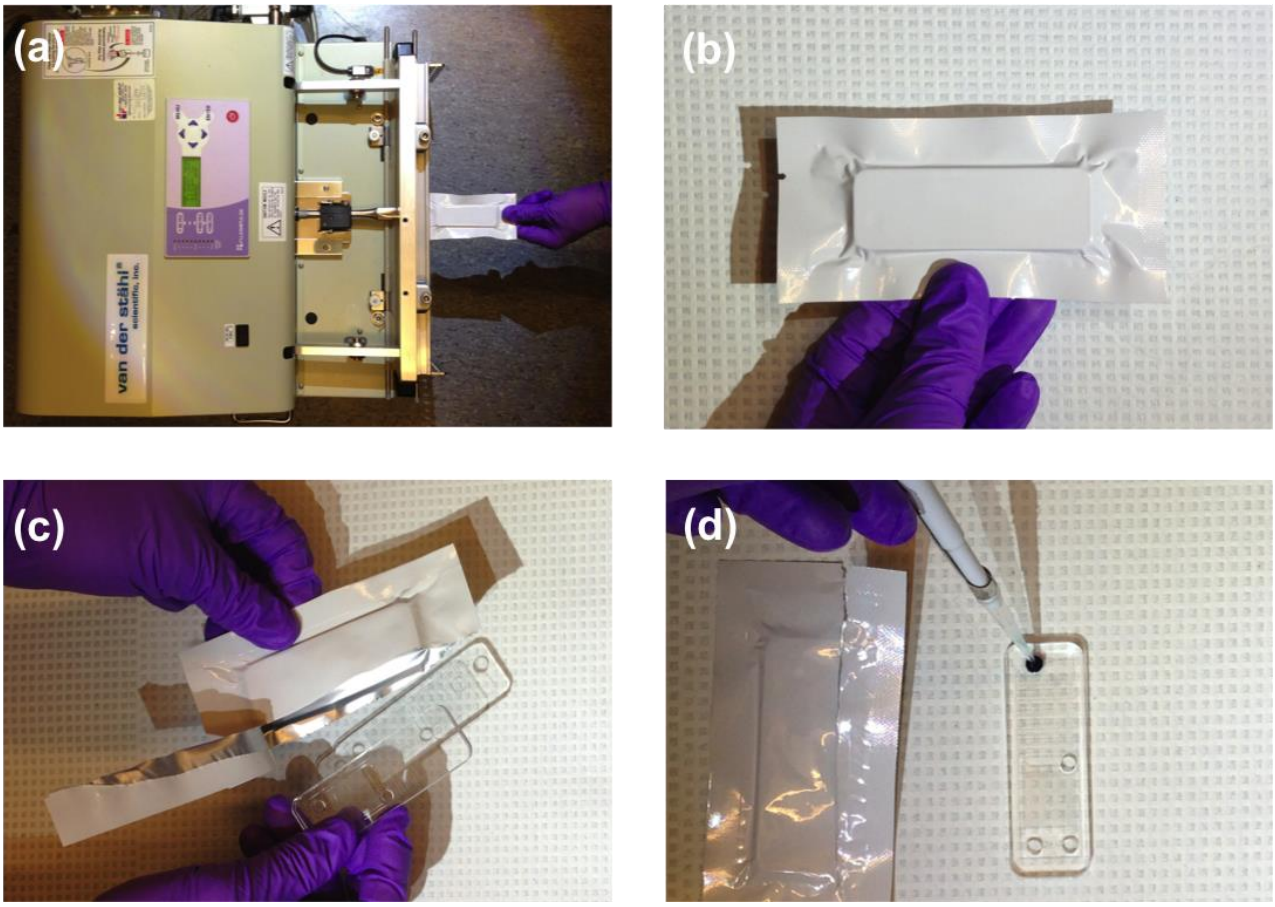

fig. S2. Vacuum charging and long-term storage. (**a**) After the chips are incubated in vacuum overnight (-95 kPa), it is sealed in an aluminum pouch with a vacuum sealer. It takes only several seconds to seal each pouch. There is a layer of plastic laminated on the inside of the aluminum seals, and by heating the seams up, the vacuum sealer can melt and seal the pouch. (**b**) Zoom in on the sealed pouch. This pouch can be stored indefinitely and transported easily to remote areas. (**c**) The user simply rips the seal open and load samples in. (**d**) Loading of the samples (food dye). With the vacuum battery system, there is a long operation window of ~2.5 hours for the user to load the chip.

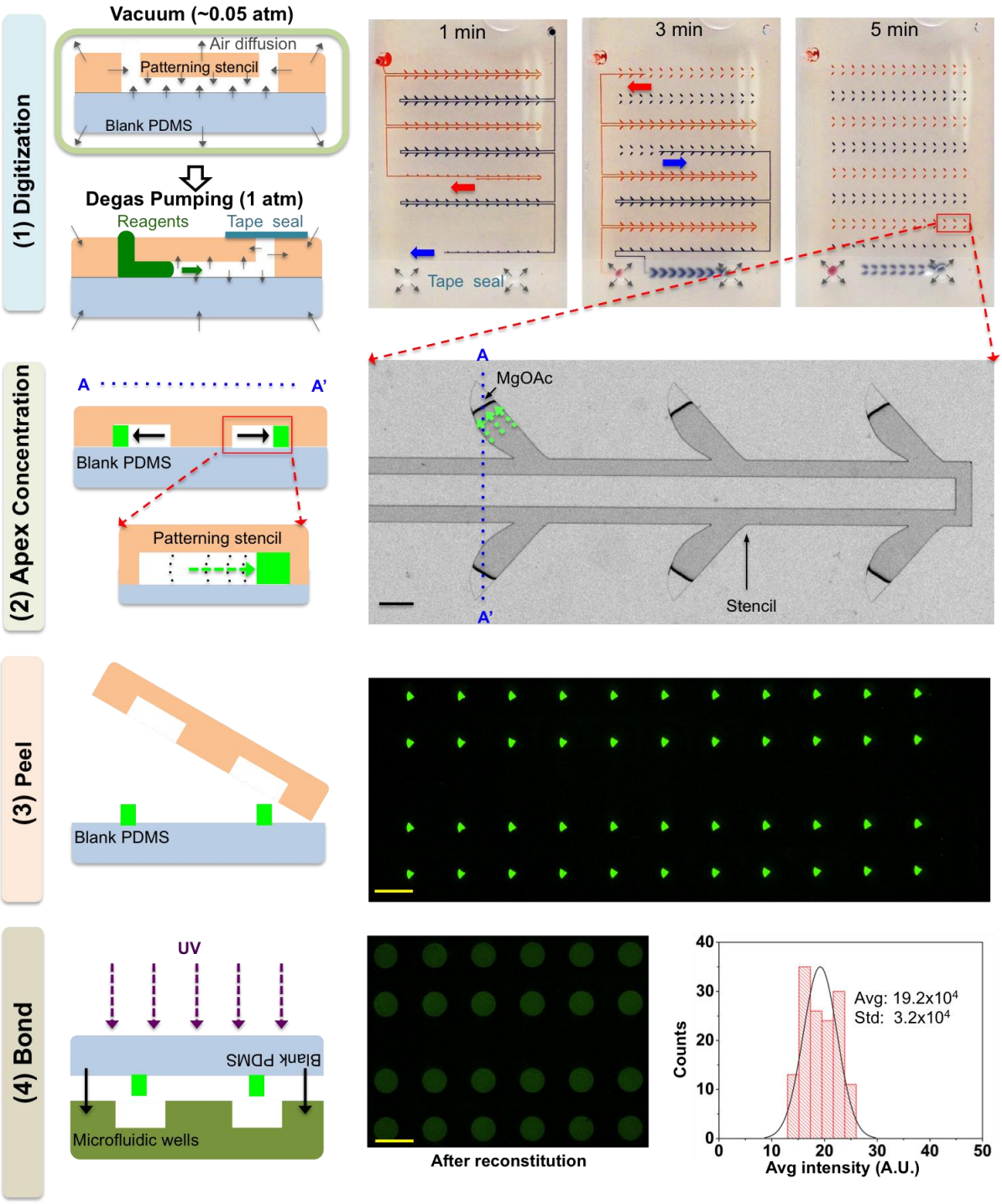

fig. S3. Detailed steps of micropatterning. (**1**) Degas pumping draws reagents (food dye) into the stencil and a trailing air gap compartmentalizes the reagents into individual leaf-shape patterns. (**2**) Micro-apex concentrating can be done by simple air drying. (**3**) The stencil is peeled away, and can be reused after washed. The MgOAc (with fluorescein for visualization) sticks to the hydrophilic (oxygen plasma treated) bottom blank PDMS. (**4**) Bonding is done by UV treatment and manual alignment. Right graph shows intensity distribution after reconstituting the wells with water.

note S1. Simulation of particle trajectories.

We used COMSOL Multiphysics software to simulate the flow profile and particle trajectories. The first step was to simulate the fluid flow through the microfluidic device. The flow can be described with the Navier-Stokes equations *(53)*. We assumed incompressible flow and steady state laminar flow (Reynolds number <1). We applied no-slip boundary conditions to the walls. We used the single-phase laminar flow module in COMSOL to simulate the flow field.

Next we used the flow field results and simulated the particle trajectories using the Particle Tracing for Fluid Flow module. The forces that the blood cells experience are drag and gravity forces. The total force experienced on each particle is the sum of drag forces and gravity forces. For simplicity, we approximated the blood cells as spheres, and assumed it experienced Stokes drag. Gravitation force is the main force that causes the blood cells sedimentation and allow for plasma skimming on the top edges of the main channels. Finally, the particle momentum can be described with Newton's second law, the rate of change of its momentum is equal to the net force the particle experiences. Using these equations, and the previously simulated flow field, we simulated the particle trajectories in a time dependent model. We calculated the separation efficiency as the ratio of blood particles removed from the microwells. The simulation result is shown in Fig. 3E in dashed lines.

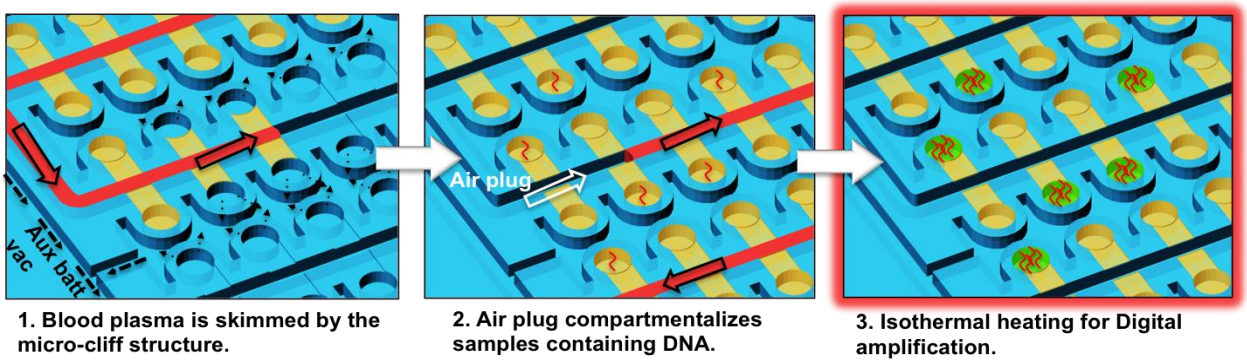

fig. S4. Digital plasma separation mechanism overview. (**1**) Air diffuses across the PDMS walls into the battery void, sucking samples in. Plasma is skimmed into microwells by the microcliff. (**2**) An trailing air plug enters and compartmentalizes the micorwells at the end of loading. Target nucleic acid (red S shapes) is distributed with a Poisson distribution. (**3**) RPA is commenced in each microwell and the number of amplified fluorescing microwells correlates to the original target concentration.

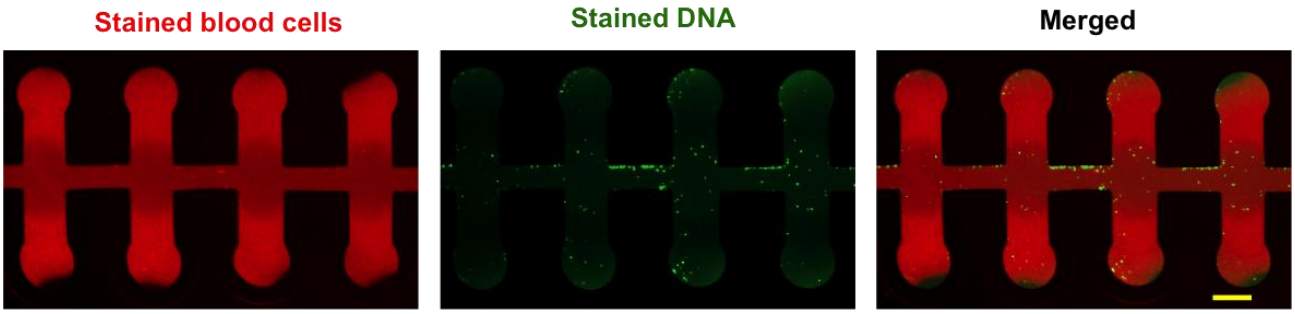

fig. S5. Failure of blood separation without the microcliff. Here the entire fluidic design height was at h_1=h_2=300 μm (see Fig.3b for definition of h_1,h_2), no microcliff was present. Fluorescence images show human blood mixed with stained DNA. Blood cells tend to obscure DNA readout if it is not separated. There was a slightly higher concentration of blood cells in the microwells than the main channel, contributing to the negative separation efficiency. This is likely due to inertial effects. Contrast normalized. Scale bar=500 μm.

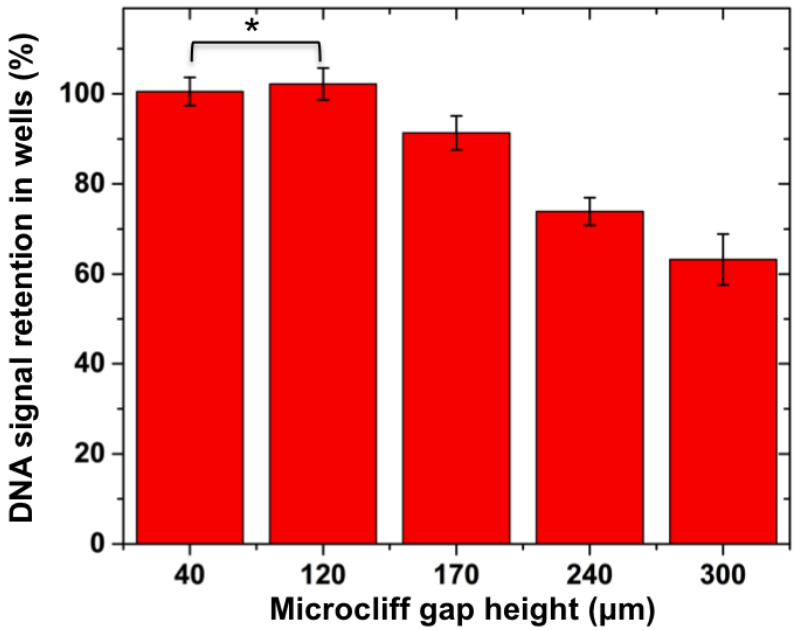

fig. S6. Optical signal obstructed when blood cells are not removed. The quantitative results show that smaller microcliff gaps can allow higher fluorescence signal from stained DNA because of better blood cell separation. Flow rate across microcliff was kept at 3 nl min^{-1}. Flow rate in the main channel was 5 μl min^{-1}. (mean ± s.d., *not significantly different, all other pairs were significantly different with $p<0.05$, one-way ANOVA Sidakholm test, n=6)

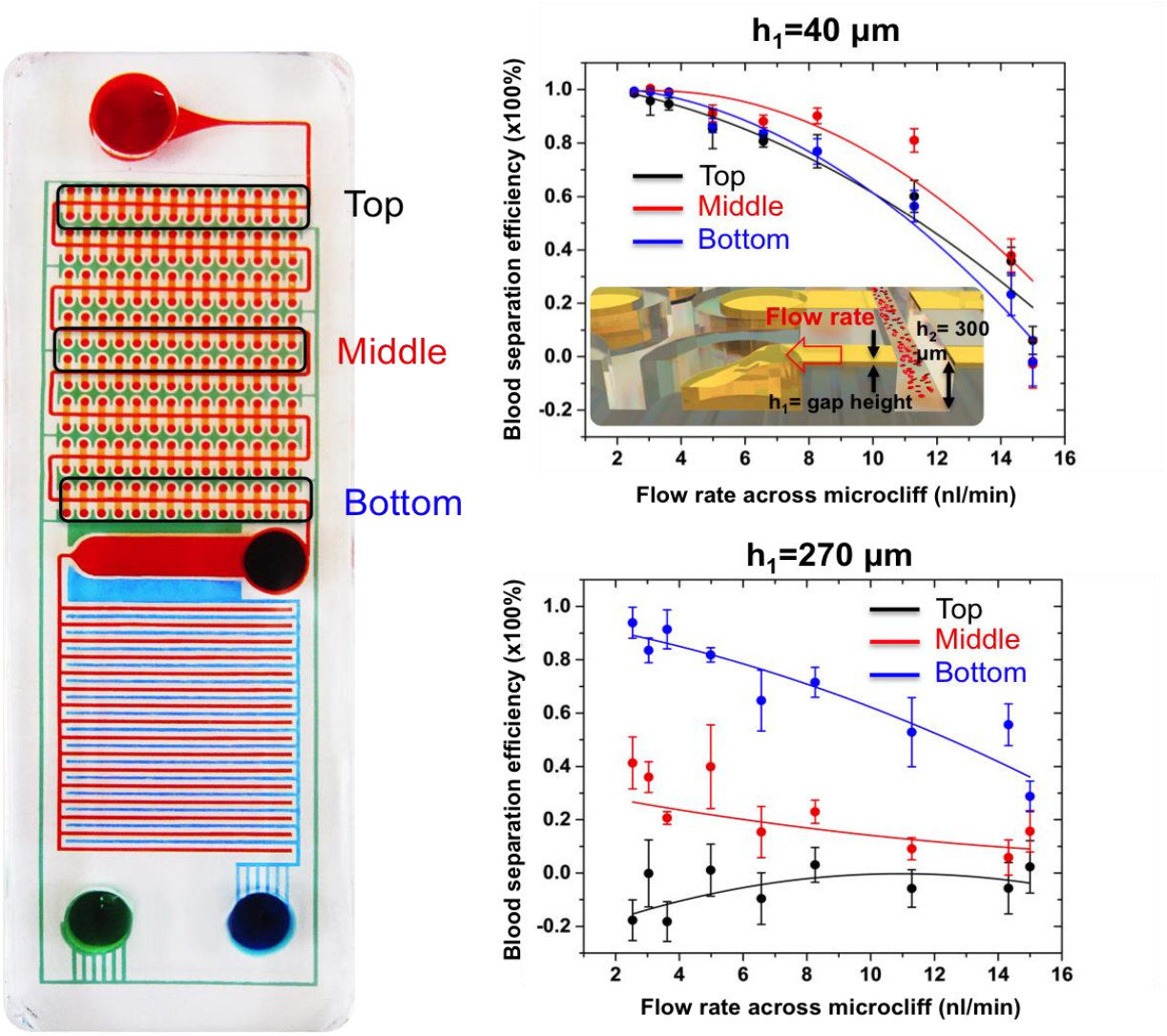

fig. S7. Microcliff gap effect on spatial robustness. When the gap size of h_1 increases, the separation efficiency in the top wells near the inlet have very poor blood separation efficiency, this is because the blood cells do not have sufficient time to sediment in the main flow channel and get sucked into the wells. On the other hand, there is much less variation among top, middle, and bottom well separation efficiencies with a smaller microcliff gap design. (mean ± s.d., n=6 for all data points)

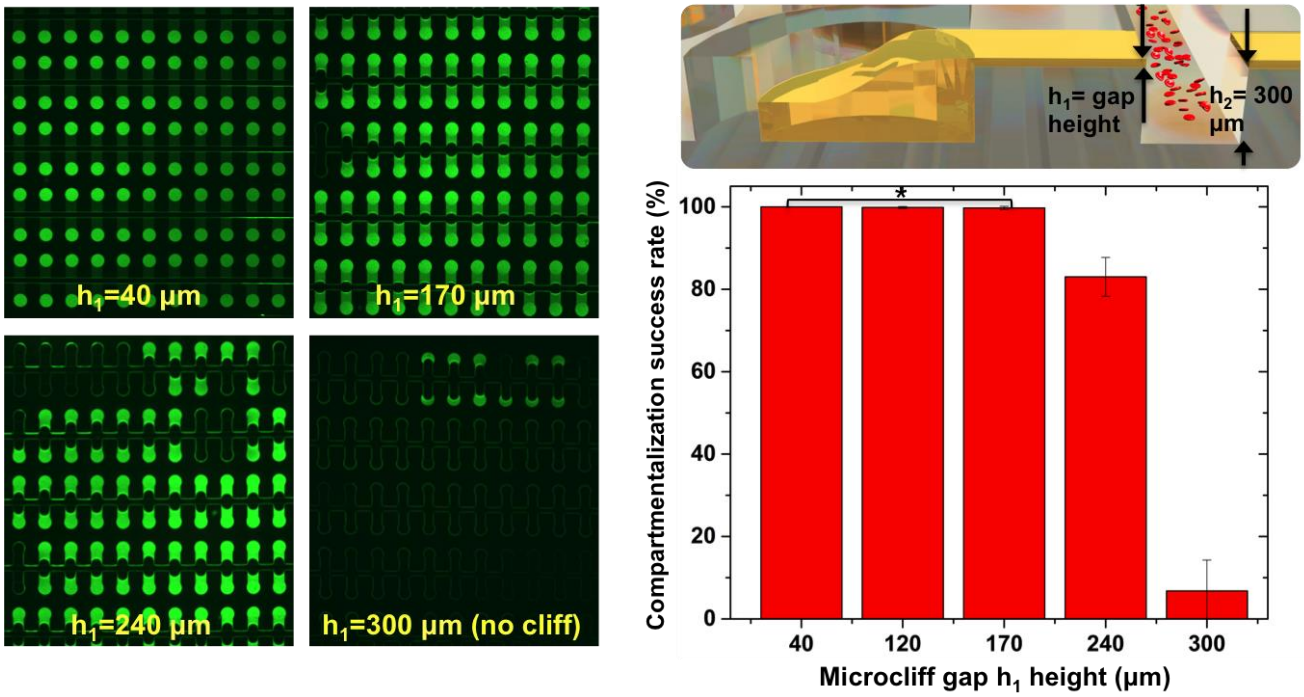

fig. S8. Reliable compartmentalization with smaller microcliff gap designs. Successful compartmentalization is defined as complete filling and retaining of liquids within a microwell after the air gap recedes and separates each well. An aliquot of 110 µl of human blood (20% blood in PBS) spiked with fluorescein was loaded into chips with different microcliff gap heights (h_1). (mean ± s.d., *not significantly different (40, 120, and 170 µm), all other pairs were significantly different with each other $p<0.05$, one-way ANOVA Sidakholm test, n=224 for all sets). We avoided cross-contamination of amplified targets since the sample is being continuously sucked into the microwells by the vacuum battery, so fluid flows into the microwells. Also, we fine-tuned the amount of input sample volume so the air gap compartmentalizes all microwells immediately when the wells are almost fully loaded, thus preventing backflow and cross contamination. In addition, unlike conventional microfluidic chips, a unique attribute of the vacuum battery system is that it removes any air bubbles that may arise during heating, hence removing the risk of catastrophic expulsion of cross-contaminating samples during heating incubation. Also, at room temperature the amplification kinetics is significantly slower. Finally, we observed there was no streaking, no inflation of positive wells especially at low concentrations, and fairly consistent results of our experiments (Fig. 5), so we conclude that there is minimal cross contamination.

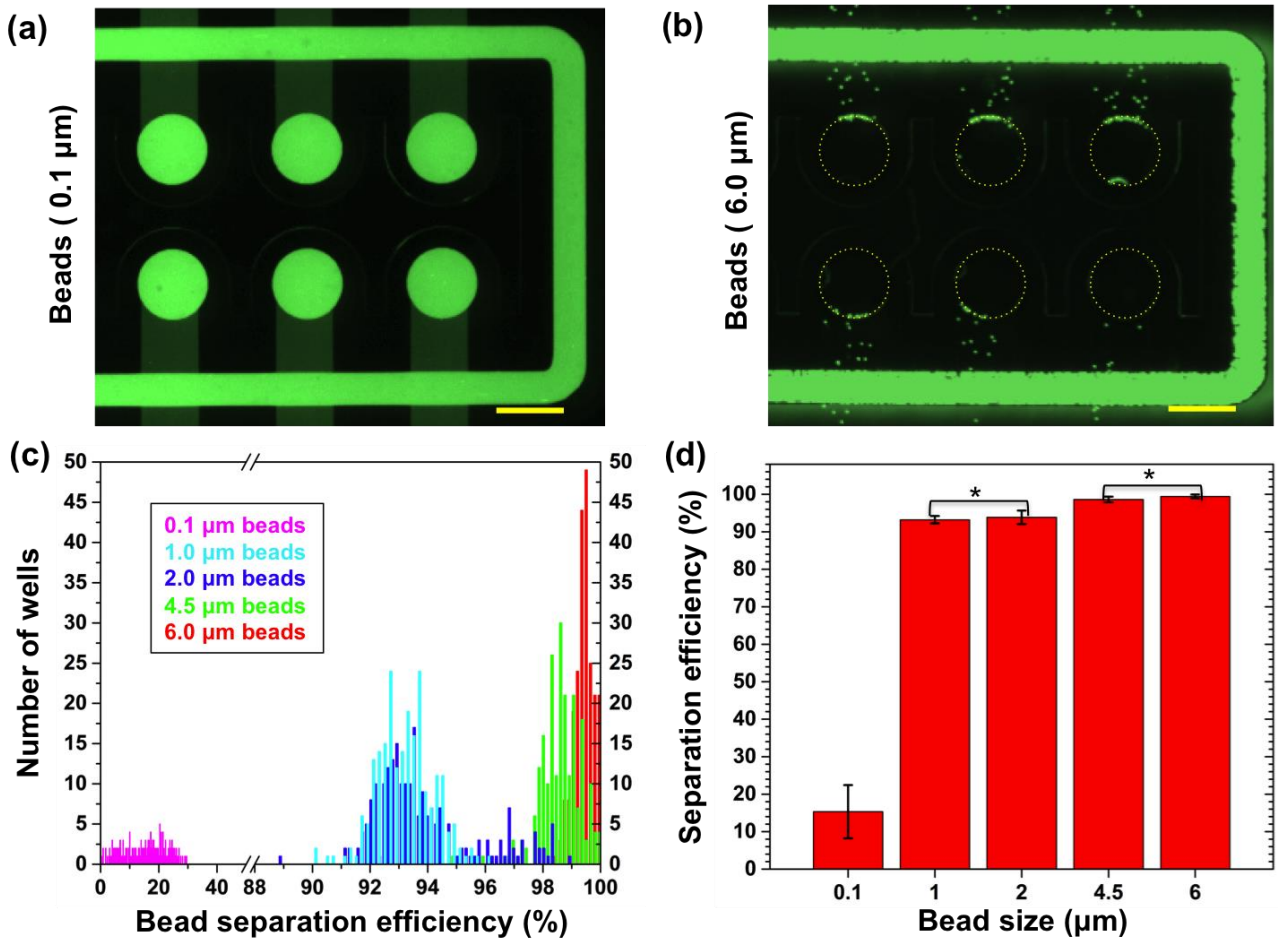

fig. S9. Selective particle separation according to size. We tested the 40 µm micro-cliff gap design to separate different sizes of polystyrene particles. We found that it was capable of separating >99% of 6 µm beads (which are similar size to red blood cells), while retaining >85% of the 0.1 µm beads (which are similar size to some viruses). Beads were polystyrene microspheres diluted in PBS. (**a**) and (**b**) show actual fluorescence pictures of bead separation results. Dashed yellow circles depict where the microwells are located. (**c**) Shows the histogram results and (**d**) shows the mean. Separation efficiency is defined as 1-(intensity in wells-background)/(intensity in main flow channel-background). (mean ± s.d., *not significantly different, all other pairs were significantly different with each other $p<0.05$, one-way ANOVA Sidakholm test, n=224 for all sets. Scale bar is 650 µm).

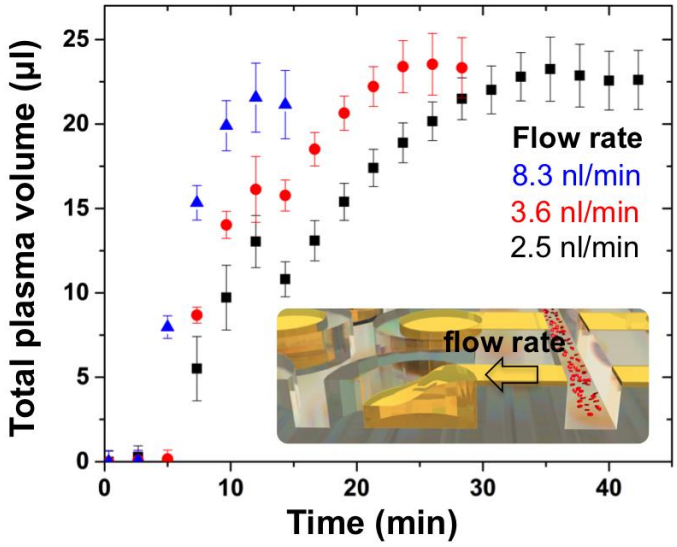

fig. S10. Total plasma volume separated versus time. There are a total of 224 wells, each having a volume of 100 nl, which fills with plasma simultaneously. We varied the flow rate into the wells by controlling the negative pressure applied to the auxiliary vacuum battery. This data was taken from 40 µm microgap devices. Plasma separation could be finished within 12 minutes. (mean ± s.d., n=6)

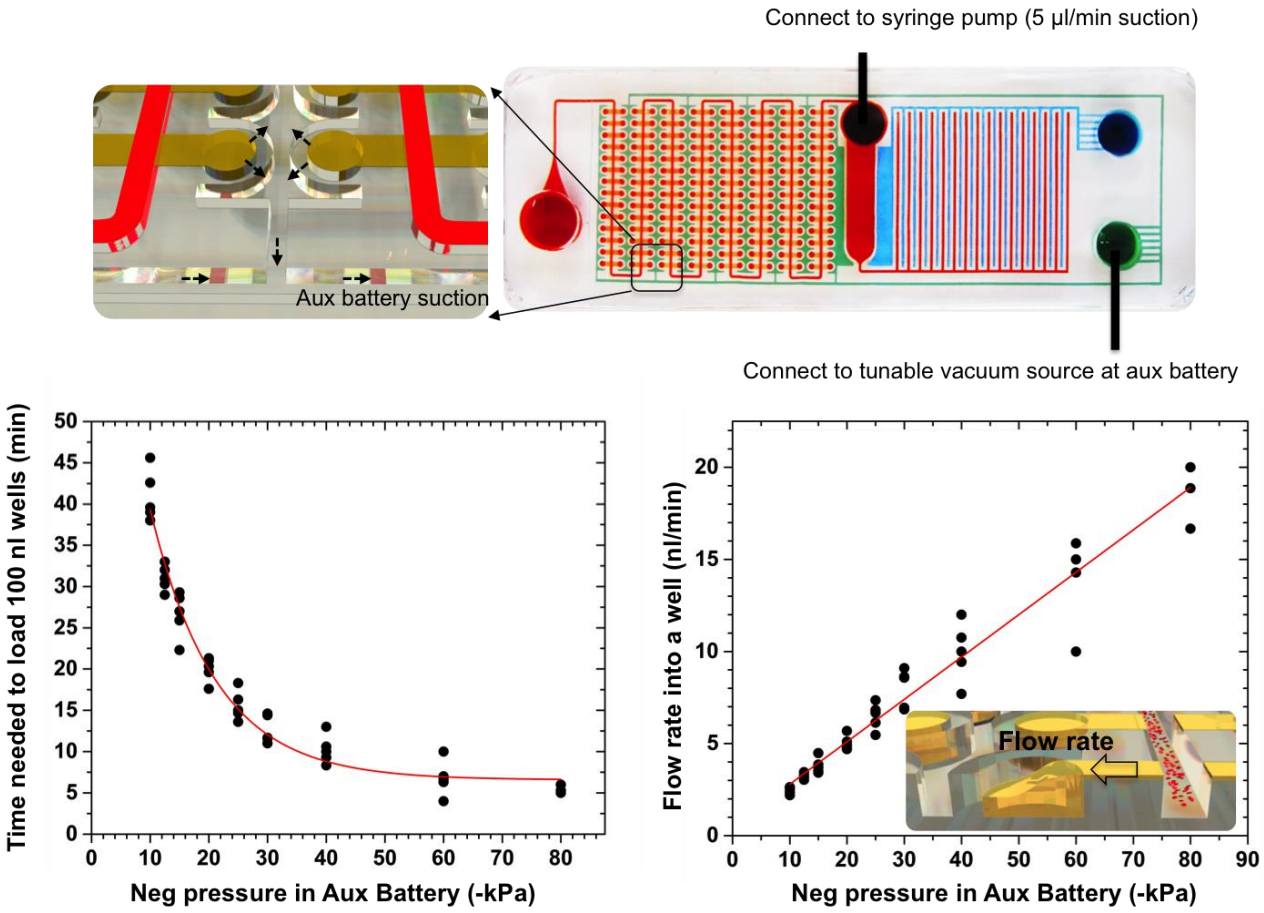

fig. S11. Microwell filling speed versus vacuum strength. This was the experimental setup for data sets involved with calibrated flow rates across microcliff gaps. We connected a vacuum source directly to the auxiliary battery and applied variable vacuum pressure to characterize the effect on microwell filling speed. Flow through the main channel was kept constant using a syringe pump. Black dots denote experimental results. Red curve denotes fitting results. The left figure was fitted with an exponential decay function (Adj. R-Square=0.97). The right figure was fitted with a liner function (Pearson's r=0.98). n=5.

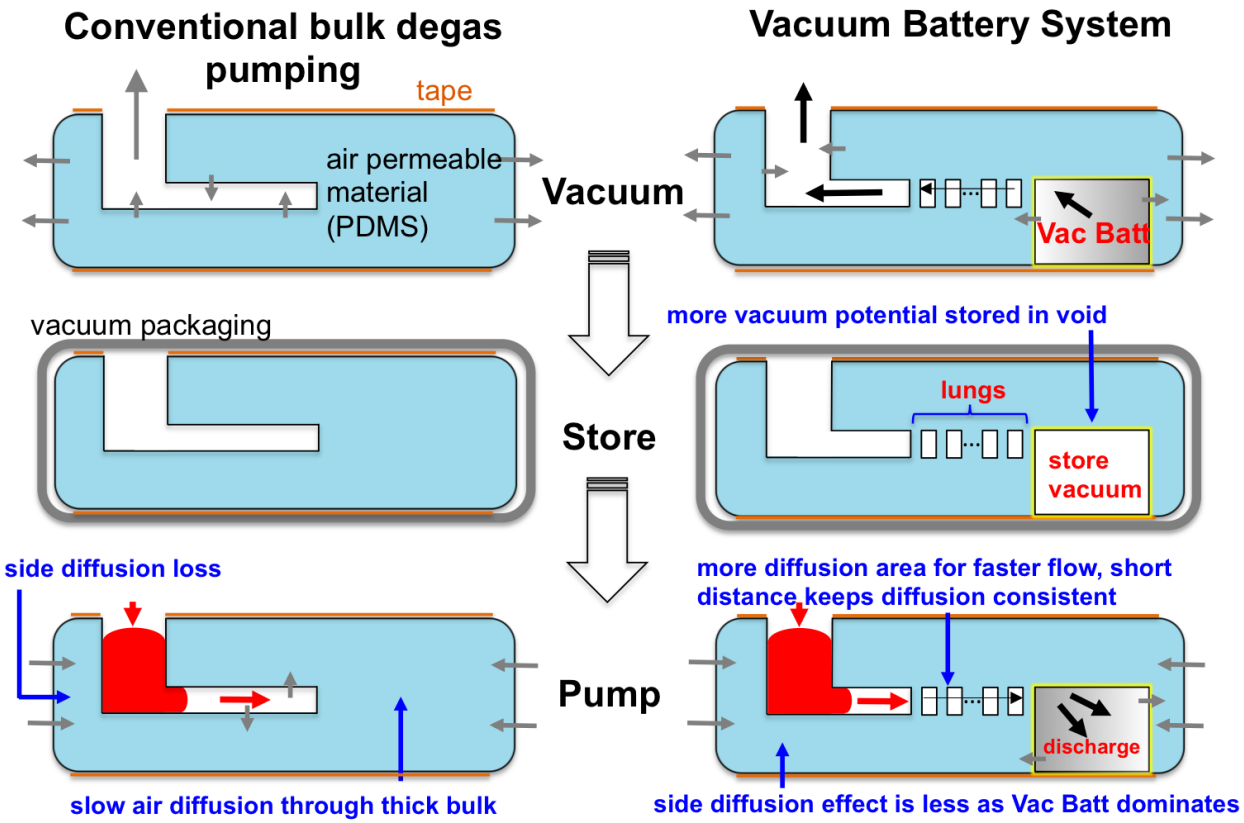

fig. S12. Vacuum battery system versus conventional degas pumping. The vacuum battery system provides more reliable flow, faster flow, and longer operation time compared to conventional bulk degas pumping.

note S2. Diffusion through vacuum battery.

The air diffusion across from the fluid channels through the PDMS vacuum lungs into the vacuum battery space can be described with Fick's second law (*54,55*). The air pressure in the fluid channels and in the vacuum battery void can be found by correlating the gas concentration via the ideal gas law. The volume of liquid being sucked in the device is the same volume of air that has diffused into the vacuum battery and PDMS. This volume can be calculated by integrating the flux of air concentration being degassed over time and surface area.

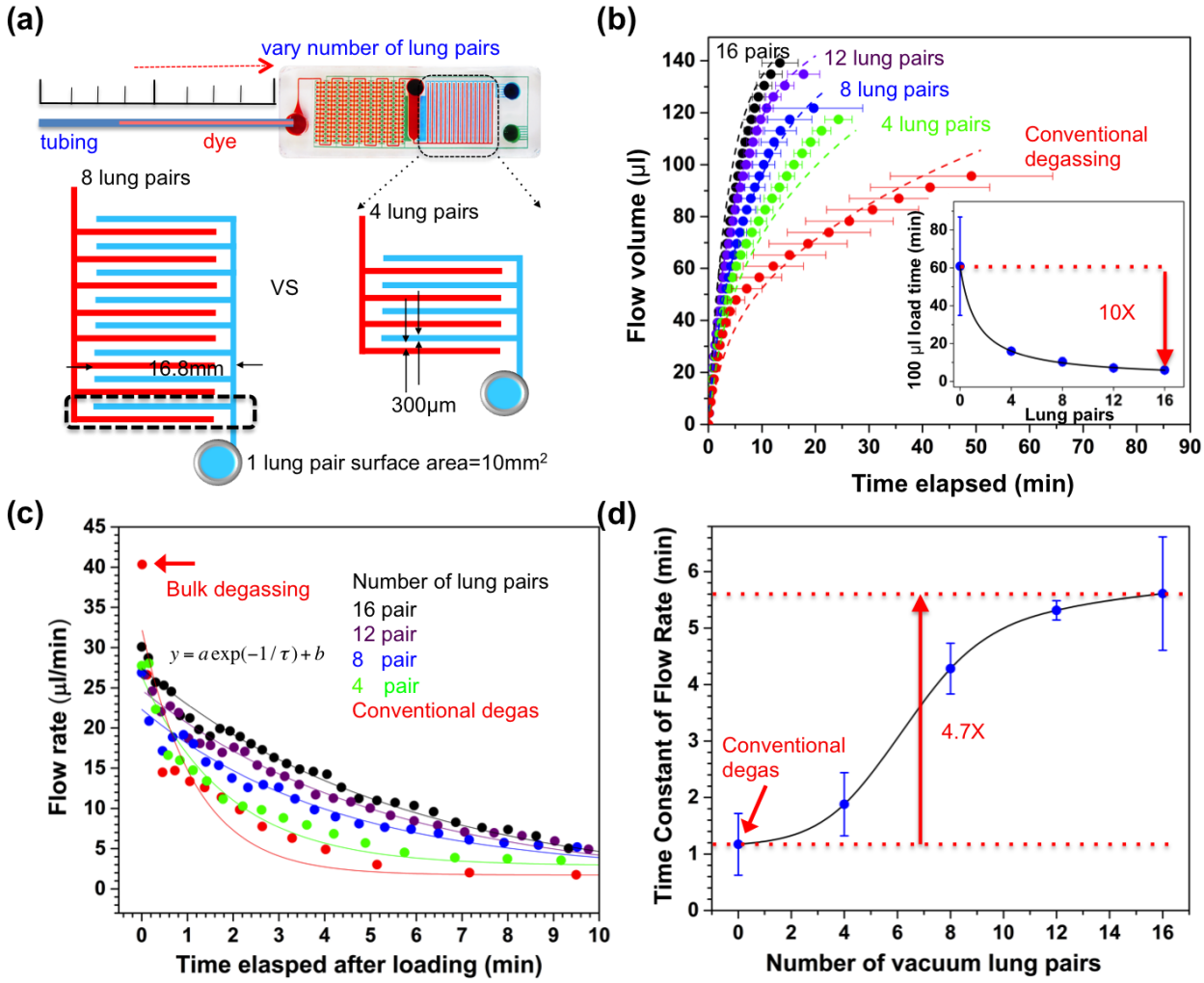

fig. S13. Vacuum lungs enable flow tuning. (**a**) and (**b**), flow rate can be also easily tuned by changing the number of lung pairs, which change the air diffusion surface area. Time gap was 5 minutes. Dashed lines are simulation results. Solid dots show experimental results. Solid line in inset depict an inverse fitting function ($y=a+b*(x+c)^{-1}$, mean ± s.d., Adj. R-Square=0.99, and $p<0.01$ (ANOVA), n=3). (**c**) Flow rates decay slower with the vacuum battery system when there are more lung pairs. Time gap out of vacuum=15 min, (**d**) Exponential decay time constant is 5 times slower with the vacuum battery system compared to conventional degas pumping. The flow rate was extracted from the derivative of flow volume vs. time. Originpro software was used to extract the derivatives and also fit the flow rate with exponential decay curves. For all experiments, both main and aux vacuum batteries were kept constant at 100 µl, mean ± s.d., n=3.

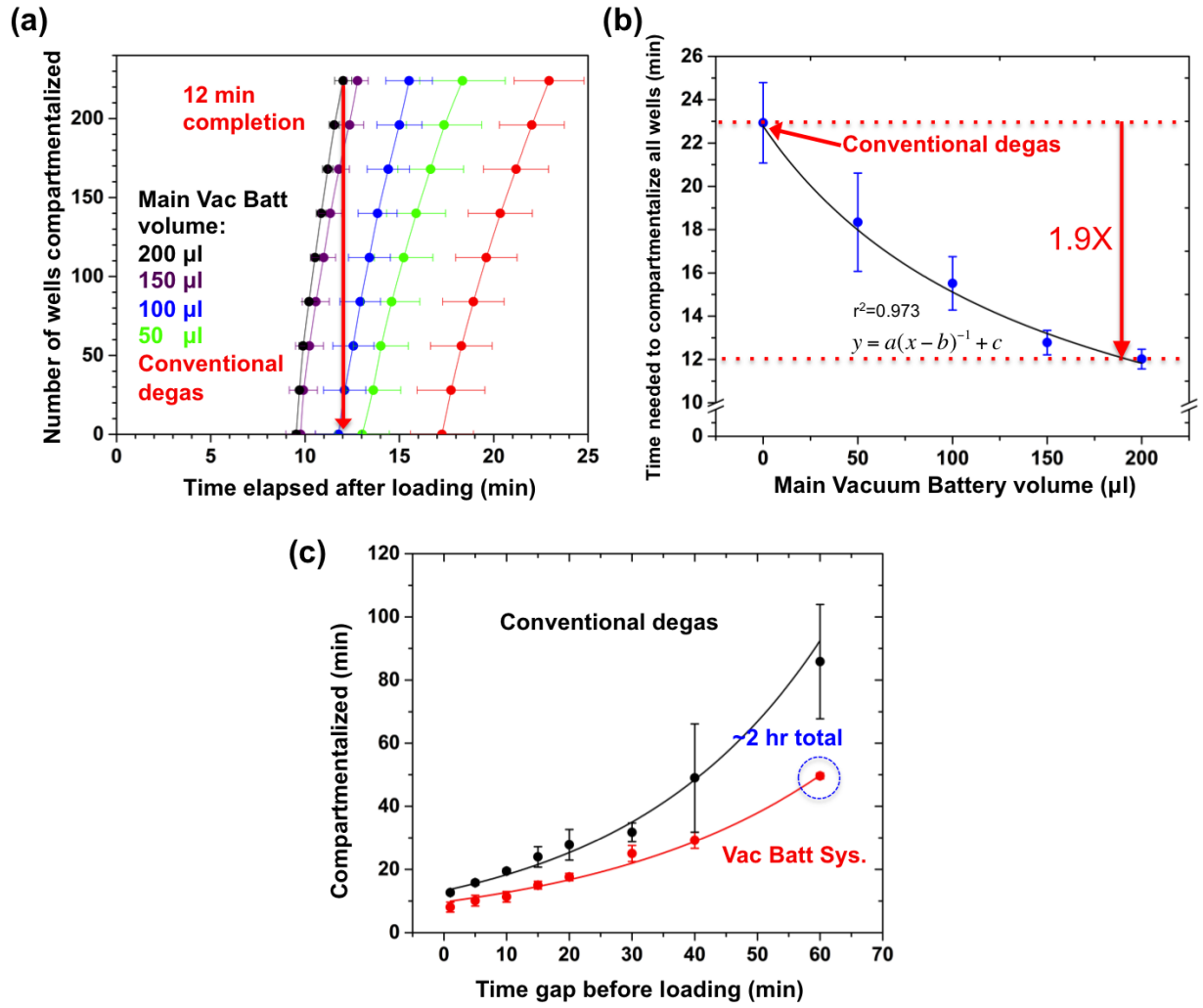

fig. S14. Compartmentalization of all 224 microwells can be done in 12 min. (**a**) The main battery volume was varied and auxiliary battery was kept constant at 100 µl for all groups (except for conventional degas, there were no main and aux battery). (**b**) We found there is an inverse relationship between compartmentalization time and vacuum battery volume. Time gap out of vacuum was 15 minutes. The 40 µm microcliff gap chip was used. (mean ± s.d., n=3). The speed and vacuum battery size was not directly proportional because pumping is a summation of degassing from the bulk PDMS, plus the air diffusion across vacuum lungs into the vacuum battery. (**c**) We also tested the effect on complete compartmentalization (224 wells) by varying the time gap that the chip is left idle out of vacuum. The vacuum battery system was always faster and more consistent than conventional degas pumping. We fitted the data with an exponential function y=a*exp(b*x), we found Adj. R-Square was 0.99 (conv. degas), 0.92 (vac batt sys.), and P<0.01 (ANOVA). (mean ± s.d., n=3, main and aux battery both at 100 µl).

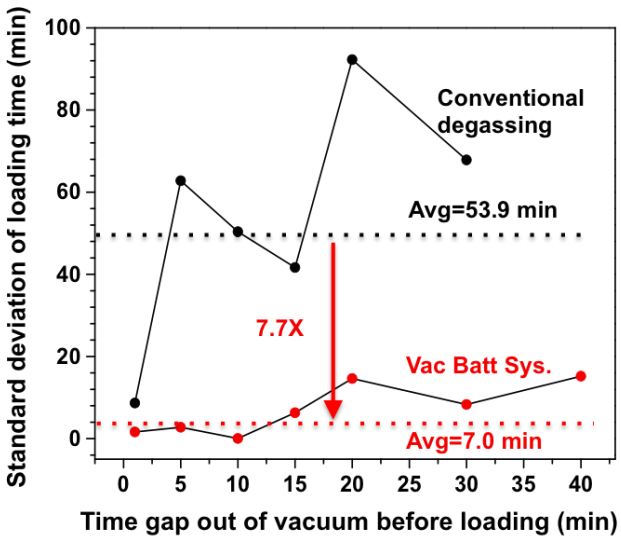

fig. S15. Consistent loading with the vacuum battery system. The end-loading standard deviation was compared with conventional degassing (from Fig. 4f). Regardless of the time gap out of vacuum, the vacuum battery system was more consistent.

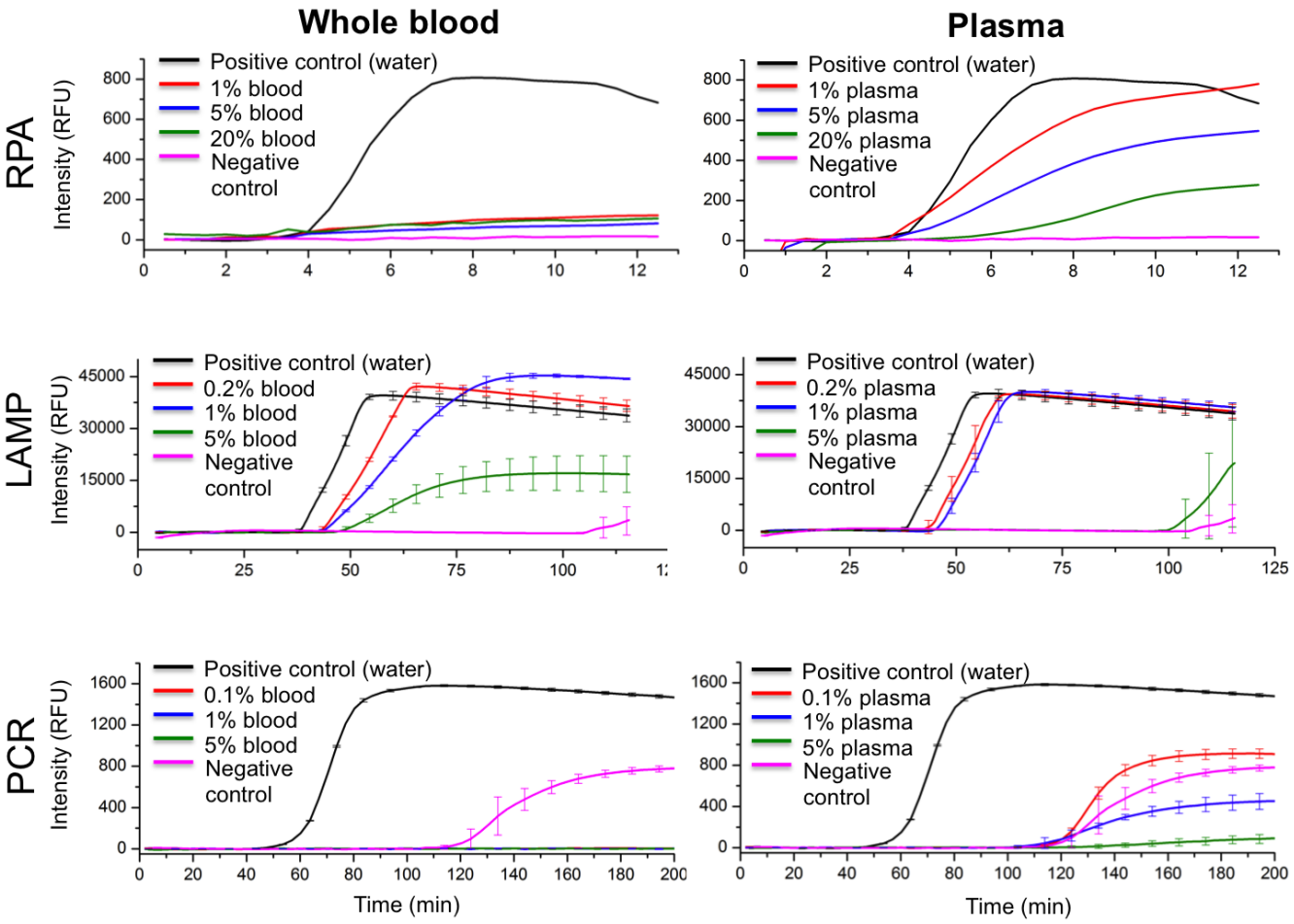

fig. S16. RPA is more robust against plasma samples than LAMP and PCR. We performed off-chip tests to determine the robustness of each nucleic acid amplification technique. Positive control had templates spiked in water, and negative control had no template spiked in water. The best case was demonstrated by RPA in plasma. Amplification directly from blood was generally very difficult. RPA also showed an extremely fast reaction rate, where the fluorescence signal starts to show up in 4 minutes. In addition, RPA showed much higher tolerance and remained functional at higher plasma concentrations. LAMP was able to amplify in some blood, but only up to 5% and gives false positives. On the other hand, the negative control in RPA never gave false positive signals. Due to these reasons, we decided to use RPA to demonstrate the utility of our microfluidic plasma separation platform. We used the RPA-exo kit for experiments. Data was collected by a real-time PCR machine (CFX-96, BioRad).

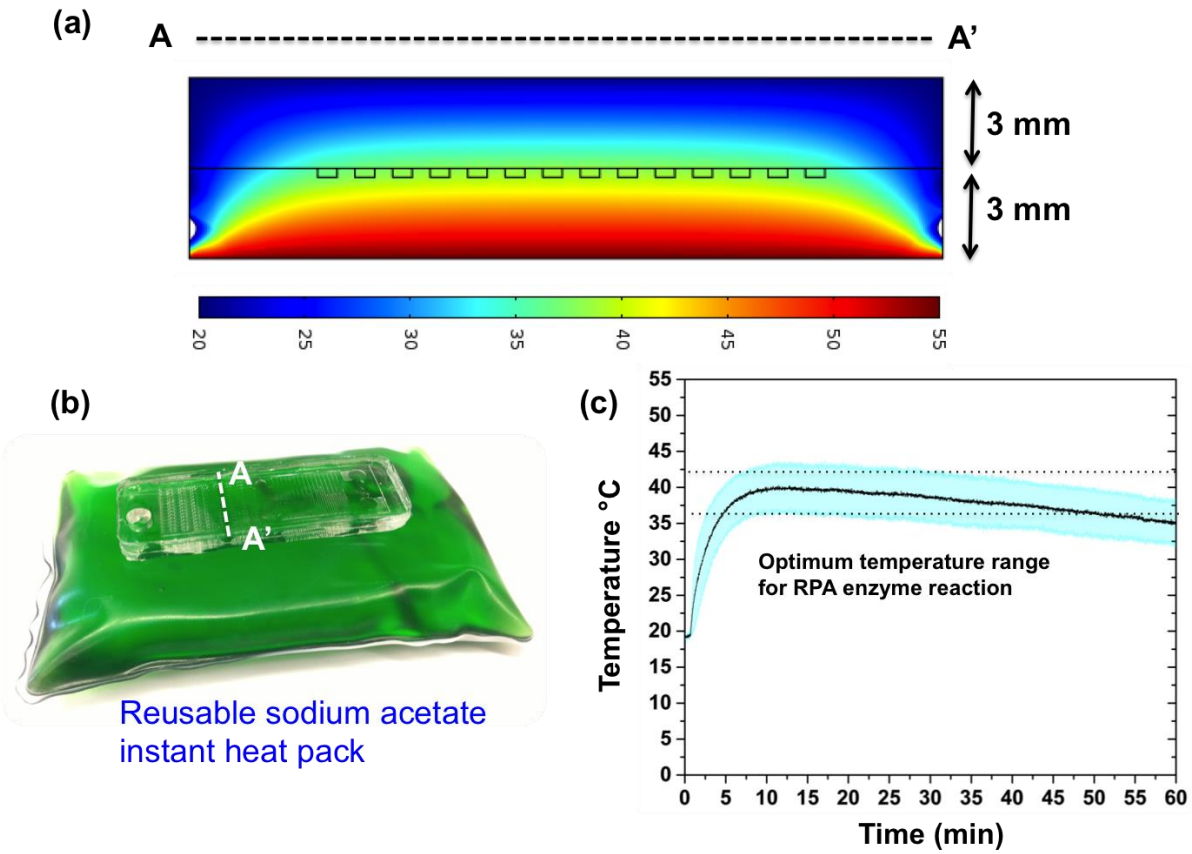

fig. S17. Isothermal heating using reusable instant heat packs. (**a**) We optimized the chip's thickness (3 mm on both top and bottom PDMS) to achieve ~40°C heating inside the wells at 25°C ambient temperature using an instant heat pack. A heating profile was simulated with COMSOL software using the heat transfer module. (**b**) A commercial reusable instant heat pack (Hotsnapz, ~$5 each) was used. The sodium acetate heat pack can be reused after soaking in boiling water for ~10 mins. Heating is caused by the exothermic phase change crystallization of super saturated sodium acetate. We ran our digital amplification reactions by simply putting our chips onto a heat pack for 20~60mins. (**c**) We observed ~40 °C heating for up to an hour using the heat packs. Since digital amplification is an end-point readout technology, the platform is very robust against temperature variation because only the saturated fluorescence signal is read. We only need a distinguishable signal between a negative well and a positive well. The intensity of the positive well does not matter since it will be counted as one well as long as it has signal distinguishable from background. RPA reactions can still commence at a lower rate at room temperature so one would simply wait slightly longer before taking an endpoint count of the positive wells. A more detailed analysis of sodium acetate heating and robustness of RPA amplification can be found in *(56)*. These heat packs are available commercially for only few dollars each. At 40°C, this temperature range will also work with other isothermal amplification technologies such as NASBA, SMART, SDA, BAD AMP. n=3, mean ± s.d..

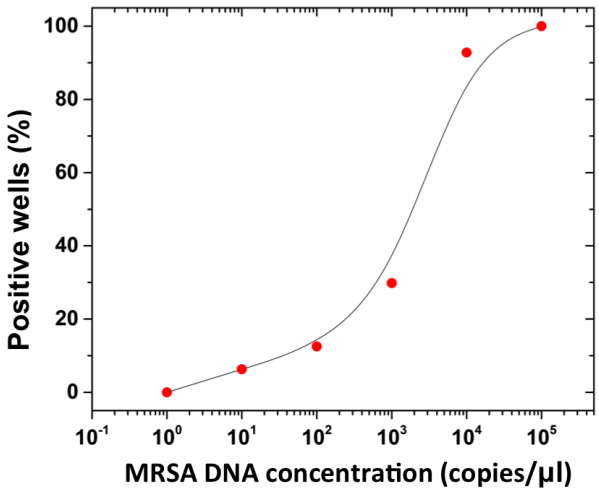

fig. S18. On-chip digital quantitative detection of MRSA DNA spiked in water. We followed the same procedures of testing in Fig. 5c, except that the matrix was in water rather than human blood. The sensitivity was slightly higher as there was less interference of the plasma components. This demonstrates that the device has potential to be used as a replacement of real-time PCR machines for general quantification of DNA concentration or water quality monitoring applications.

table S1. Primer, probe, and target sequences. Primers and target sequence ordered from Integrated DNA Technologies.

MRSA Forward primer (sccI/II)	**CTCAAAGCTAGAACTTTGCTTCACTATAAGTATTC**
MRSA Reverse Primer (orfX)	**CCCAAGGGCAAAGCGACTTTGTATTCGTCATTGGCGGATCAAACG**
MRSA II Probe sequence	**TGTTAATTGAACAAGTGTACAGAGCATT-T(FAM)-A-dSpacer-GA-T(BHQ-1)-TATGCGTGGAG** (ordered from Biosearch Technologies)
MRSA II target sequence	TTTAGTTGCAGAAAGAATTTT**CTCAAAGCTAGAACTTTGCTTCACTATAAGTATTC**AGTATAAAGAATATTTCGCTATTATTTACTTGAAATGAAAGACTGCGGAGGCTAACTATGTCAAAAATCATGAACCTCATTACTTATGATAAGCTTCTTAAAAACATAACAGCAATTCACATAAACCTCATATGTTCTGATACATTCAAAATCCCTTTATGAAGCGGCTGAAAAAACCGCATCATTTATGATATGCTT***CTCCACGCATAATCTTAAATGCTCTGTACACTTGTTCAATTAACA***CAACCCGCATCATTTGATGTGGGAATGTCATTTTGCTGAATGATAGTGCGTAGTTACTGCGTTGTAAGACGTCCTTGTGCAGGC**CGTTTGATCCGCCAATGACGAATACAAAGTCGCTTTGCCCTTGGG**TCATGCG
HIV primers and probes	provided by Twistdx, probes are FAM probes for the RPA RT-exo kit.
HIV RNA	Seracare, 500405, Purified RNA, HIV-1 Group M, Subtype B